

Direct numerical simulation of turbulent boundary layer with fully resolved particles at low volume fraction

Cite as: Phys. Fluids **29**, 053301 (2017); <https://doi.org/10.1063/1.4982233>

Submitted: 19 December 2016 . Accepted: 13 April 2017 . Published Online: 04 May 2017

Kun Luo, Chenshu Hu, Fan Wu, and Jianren Fan

COLLECTIONS

 This paper was selected as Featured



[View Online](#)



[Export Citation](#)



[CrossMark](#)

ARTICLES YOU MAY BE INTERESTED IN

Buoyancy effects in an unstably stratified turbulent boundary layer flow
Physics of Fluids **29**, 015104 (2017); <https://doi.org/10.1063/1.4973667>

Direct numerical simulation of flow around a surface-mounted finite square cylinder at low Reynolds numbers

Physics of Fluids **29**, 045101 (2017); <https://doi.org/10.1063/1.4979479>

On the shape memory of red blood cells

Physics of Fluids **29**, 041901 (2017); <https://doi.org/10.1063/1.4979271>



CAPTURE WHAT'S POSSIBLE
WITH OUR NEW PUBLISHING ACADEMY RESOURCES

[Learn more](#) 

AIP Publishing

Direct numerical simulation of turbulent boundary layer with fully resolved particles at low volume fraction

Kun Luo, Chenshu Hu, Fan Wu, and Jianren Fan^{a)}

*State Key Laboratory of Clean Energy Utilization, Zhejiang University, Hangzhou 310027,
People's Republic of China*

(Received 19 December 2016; accepted 13 April 2017; published online 4 May 2017)

In the present work, a direct numerical simulation (DNS) of dilute particulate flow in a turbulent boundary layer has been conducted, containing thousands of finite-sized solid rigid particles. The particle surfaces are resolved with the multi-direct forcing immersed-boundary method. This is, to the best of the authors' knowledge, the first DNS study of a turbulent boundary layer laden with finite-sized particles. The particles have a diameter of approximately 11.3 wall units, a density of 3.3 times that of the fluid, and a solid volume fraction of 1/1000. The simulation shows that the onset and the completion of the transition processes are shifted earlier with the inclusion of the solid phase and that the resulting streamwise mean velocity of the boundary layer in the particle-laden case is almost consistent with the results of the single-phase case. At the same time, relatively stronger particle movements are observed in the near-wall regions, due to the driving of the counterrotating streamwise vortices. As a result, increased levels of dissipation occur on the particle surfaces, and the root mean square of the fluctuating velocities of the fluid in the near-wall regions is decreased. Under the present parameters, including the particle Stokes number $St^+ = 24$ and the particle Reynolds number $Re_p = 33$ based on the maximum instantaneous fluid-solid velocity lag, no vortex shedding behind the particle is observed. Lastly, a trajectory analysis of the particles shows the influence of turbophoresis on particle wall-normal concentration, and the particles that originated between $y^+ = 60$ and 2/3 of the boundary-layer thickness are the most influenced. *Published by AIP Publishing.* [http://dx.doi.org/10.1063/1.4982233]

I. INTRODUCTION

The phenomenon of particle-laden turbulent boundary layer is widely encountered in natural environments and industrial applications, such as coal ash in boilers, pneumatic conveyance, and the transport of pollutant in rivers.^{1–3} With the addition of the particle phase, the complexity of the boundary layer is increased, and the fluid phase will be affected by the inclusion of the dispersed phase. At the same time, under these circumstances, some characteristics of the movement of the solid phase may be affected by fluid flow in the wall-bounded boundary.

To understand the particle dynamics in the turbulent boundary layer and the turbulent modulation caused by the solid phase on the fluid, experimental investigations have been carried out by researchers. Rashidi *et al.*⁴ compared the effects of large (1100 μm) and small (120 μm) polystyrene particles on the turbulence of the boundary layer. Increased wall ejections were found when the fluid is laden with larger particles, with enhanced turbulence intensities and Reynolds stresses, while smaller particles were found to have the opposite effect on the boundary layer. Rogers and Eaton⁵ introduced copper particles of 70 μm diameters into a vertical boundary layer at the position where Reynolds number based on the momentum thickness $Re_\theta = 1000$ and found substantial

damping of the fluid turbulence with the presence of the particles. The degree of the damping is shown in strong correlation with the particle concentration in the log region. Kaftori *et al.*^{6,7} carried out the experimental investigation with the same particle material as Rashidi *et al.*,⁴ and the particle diameter ranged from 100 to 900 μm . They concluded that the presence of coherent wall structures is strongly related to the particle motion and that particles are often concentrated in regions of low velocity, which are associated with wall structures. Experimental measurement in horizontal and vertical pipe showed that the particle size has a significant effect on the turbulence modulation.^{8,9} Specifically, large particles increased the fluid turbulence markedly while small particles had the opposite effect. In contrast, small particles were found to increase the higher frequency part of normalized turbulence spectrum but no distinct influence could be observed for large particles.

With the expansion of the capabilities of computation hardware, supercomputing facilities become more accessible to researchers. Direct numerical simulations (DNSs) are carried out by some researchers for the study of single-phase boundary layer. Spalart¹⁰ conducted a DNS of a zero-pressure gradient flat-plate turbulent boundary layer (ZPGFPTBL) with a spectral code, applying a periodic streamwise boundary condition, which reduced the computational length. The simulation results turned out to be an important reference for later turbulent boundary layer simulations. Wu and Moin¹¹ simulated a ZPGFPTBL from the laminar to turbulent state

^{a)}Author to whom correspondence should be addressed. Electronic mail: fanjr@zju.edu.cn. Tel./Fax: 86-571-87951764.

with the periodic introduction of isotropic patches into the fluid domain to trigger the transition. Borrell *et al.*¹² extended the ZPGFPTBL further downstream to $Re_0 = 6800$ in the Blue Gene/P architecture, which is by far the highest Reynolds number that has been achieved by researchers with DNS. While the single-phase simulation of ZPGFPTBL progressed, Sardina *et al.*¹³ presented a DNS of a spatially developing turbulent boundary layer laden with heavy particles. Two different Stokes numbers were defined based on inner and outer units of the turbulent boundary layer. Wall-normal particle concentration and streamwise velocity profiles were found to be self-similar in the outer region and were governed only by the local Stokes number based on the displacement thickness of the boundary layer. The simulation uses the one-way coupling point-particle assumption to model particle-fluid interaction, which neglects the inter-particle collisions and hydrodynamic interactions. Yamamoto *et al.*¹⁴ reported a large eddy simulation (LES) of gas-particle turbulent downward flow in a vertical channel. It is indicated by the result that, even in a relatively low particle concentration ($\sim 10^{-4}$), the effect of inter-particle interaction is not negligible, which is owing to that inter-particle interaction has great influences on preferential concentration.

Although efforts have been taken by previous studies focusing on the particle-laden turbulent boundary layer, most of the previous simulation studies^{13,15} are based on the two-way point-particle assumption in which the investigated particles are confined to a relatively small particle size. Comparatively, for larger particles, the internal mechanism of turbulence modulation by solid phase and the interaction between coherent wall structure and particle motion are still not completely understood. It should be pointed out that, no numerical investigation of finite-sized particles in the turbulent boundary layer has been reported. The present study, based on the DNS for fluid phase and particle-resolved method for solid phase, is aimed to explore turbulence modulation caused by finite-sized particles, the influence of coherent wall structure on particle motion, and preferential concentration in the ZPGFPTBL. Simulation results predicted in the present study have been compared with the previous point-particle researches. Furthermore, analysis of inter-particle collision frequency as well as the particle trajectories is performed.

II. NUMERICAL METHODOLOGY

A. Governing equations for the fluid phase

The dimensionless incompressible equations for the incompressible viscous flow in the fluid domain are

$$\nabla \cdot \mathbf{u} = 0, \quad (1)$$

$$\frac{\partial \mathbf{u}}{\partial t} + \mathbf{u} \cdot \nabla \mathbf{u} = -\nabla P + \frac{1}{Re_{\theta_0}} \nabla^2 \mathbf{u} + \mathbf{f}, \quad (2)$$

where \mathbf{u} is the fluid velocity, P is the pressure, and Re_{θ_0} is the Reynolds number based on the momentum boundary thickness θ_0 at the inlet, \mathbf{f} is the external force exerted on the fluid by the solid phase, which represents the interaction between the

particle and the fluid. It should be noted that, the inflow boundary condition of the present study is extracted from Wei's¹⁶ simulation at $Re_\theta = 800$. Hence, θ_0 is the momentum boundary thickness at the inlet in his simulation.¹⁶ All variables are non-dimensionalized by freestream velocity U_∞ and θ_0 . The momentum boundary thickness θ_0 is computed as follows:

$$\theta_0 = \left(\int_0^\delta \frac{u}{U_\infty} \left(1 - \frac{u}{U_\infty} dy \right) \right)_{inlet}. \quad (3)$$

The governing equations are solved on a non-staggered grid and a fourth-order compact finite difference scheme¹⁷ is adopted to discretize the spatial derivatives. By applying the divergence operator to the momentum equations, the pressure-Poisson equation is derived to replace the continuity equation, which is discretized with fourth-order accuracy.¹⁸ The temporal integration scheme¹⁹ is applied for time-marching in order to reduce the memory required for simulation.

B. Governing equation for the solid phase

In the present simulation, 1200 spherical particles are consistently kept freely moving in the computational domain, corresponding to a volume fraction of 1/1000. Different from the point-particle assumption broadly used in multiphase-flow researches, the interfaces of the particles are resolved, hence the volume effect will be taken into account. Under this framework, several techniques have been applied by some authors in order to impose the no-slip boundary condition and rigid-body motion upon the particle surfaces.^{20–23} The present simulation is carried out using a modified immersed-boundary method,²⁴ which employs a well-validated multi-direct forcing approach^{25–27} to obtain full-scale solutions for particle-laden flows. The surface of each particle is represented with multiple markers with average spacing that is approximately equal to the grid size of the computational domain. To satisfy the no-slip boundary condition for the surface of the particle, a force $\mathbf{F}_k(X_k)$ is imposed on each marker that constitutes the particle surface to modify the velocity. Here, $\mathbf{F}_k(X_k)$ is the force exerted on the marker, and \mathbf{f} in Equation (2) is the force exerted on the Eulerian mesh points adjacent to each marker, which represents the mutual interaction between the fluid and the immersed bodies. Following the spirit of the immersed-boundary method, it can be expressed as follows:

$$\mathbf{f}(x) = \int_{\Omega} \mathbf{F}_k(\mathbf{x}_k) \cdot \delta(\mathbf{x} - \mathbf{x}_k) d\mathbf{x}_k, \quad (4)$$

where $\delta(\mathbf{x} - \mathbf{x}_k)$ is the Dirac delta function, \mathbf{x}_k is the position of the marker-point set on the surface of each particle, and \mathbf{x} is the position of the computational Eulerian mesh. The discrete Dirac delta function of Peskin²⁴ is adopted and is formulated as follows:

$$\delta_h(x) = \frac{1}{h^3} \phi\left(\frac{x_1}{h}\right) \phi\left(\frac{x_2}{h}\right) \phi\left(\frac{x_3}{h}\right), \quad (5)$$

where x_1 , x_2 , and x_3 are the distances between Lagrangian marker point and Eulerian grid in x , y , and z direction, respectively.

The function $\phi(r)$ adopted in the present study is formulated as follows:²⁸

$$\phi(r) = \begin{cases} \frac{1}{12}|r|^3 - \frac{11}{56}|r|^2 - \frac{11}{42}|r| + \frac{61}{112} + \frac{\sqrt{3}}{336}(243 + 1584|r| - 748|r|^2 - 1560|r|^2 + 500|r|^4 + 336|r|^5 - 112|r|^6)^{\frac{1}{2}}, & |r| \leq 1 \\ \frac{1}{6}|r|^3 - \frac{7}{8}|r|^2 + \frac{7}{12}|r| + \frac{21}{16} - \frac{3}{2}\phi_3(|r| - 1), & 1 < |r| \leq 2 \\ -\frac{1}{12}|r|^3 + \frac{3}{4}|r|^2 - \frac{23}{12}|r| + \frac{9}{8} + \frac{1}{2}\phi_3(|r| - 2), & 2 < |r| \leq 3 \\ 0, & |r| \geq 3 \end{cases}. \quad (6)$$

Since the above process is performed for the surface markers of each particle, neighboring markers may interfere with one another due to the mutual influence of the direct forcing; as a result, the velocities at the points on the immersed boundary may not be exactly equal to the correct values. To enable the velocity on each particle surface to exactly satisfy the no-slip boundary condition, which is the main idea of multi-direct forcing, the process is iteratively repeated so that the interferer is removed. The calculation procedure is described in detail in the work of Wang *et al.*²⁷

In this simulation, the particles are spherical with diameter d_p and density ρ_p . With the direct-forcing method, the force experienced by each particle from the fluid equals to the summation of the forces of each surface marker. Throughout the simulation, particles may experience hydrodynamic forces, inter-particle collision forces, and particle-wall collision forces. As a result, the governing equations for the particle can be written as follows:

$$\frac{d\mathbf{x}_p}{dt} = \mathbf{u}_p, \quad (7)$$

$$m_p \frac{d\mathbf{u}_p}{dt} = \mathbf{F}_d + \mathbf{F}_p + \mathbf{F}_w, \quad (8)$$

$$I_p \frac{d\omega_p}{dt} = \mathbf{T}, \quad (9)$$

where \mathbf{F}_d is the hydrodynamic force, \mathbf{F}_p is the inter-particle collision force, \mathbf{F}_w is the particle-wall collision force, m_p is the mass of the particle, I_p is the moment of inertia, and \mathbf{T} is the torque acting on the particle.

Although the particle volume fraction (1/1000) can be considered dilute in the present simulation, collisions might occur when particles approach one another. A collision model based on the spirit of the soft-sphere collision model²⁹ is applied here. By contrast, hard-sphere collision model,³⁰ which can only handle binary collisions once a time, requires a very small time step when multi-particle collisions occur. Therefore, soft-sphere model is a better choice to cope with particle collision in case of the high local particle concentration in the near-wall region. In practice, we used the following equation to account for the collision forces:

$$\mathbf{F}_C = -k_n \delta_{nij} \mathbf{n}_{ij} - \eta_n \mathbf{v}_{nij}, \quad (10)$$

where k_n is the normal spring stiffness, η_n is the normal damping coefficient, δ_{nij} is the overlap between the particles, \mathbf{n}_{ij} is the unit normal vector connecting the colliding particle

centers, and \mathbf{v}_{nij} is the relative velocity between the two colliding particles. In the study, spring coefficient $k_n = 800$ N/m and restitution coefficient $e_n = 0.97$ is adopted. The viscous damping coefficient is given as follows:³¹

$$\eta_n = \frac{2\sqrt{m_p k_n} |\ln e_n|}{\sqrt{\pi^2 + \ln^2 e_n}}, \quad (11)$$

where e_n is restitution coefficient in the normal direction. The overlap δ_{nij} is calculated as

$$\delta_{nij} = r_i + r_j - |\mathbf{x}_i - \mathbf{x}_j|, \quad (12)$$

where r_i, r_j denote the radius of particle i, j and $\mathbf{x}_i, \mathbf{x}_j$ denote the location of particle i, j .

During the particles collision, the surface of one particle will slightly penetrate the surface of the other, and some of its surface markers will enter the volume of the other particle. These surface markers inside the solid region are unable to affect the fluid and are physically meaningless. Moreover, these markers will significantly influence the stability of the computation in fluid-solid coupling procedure. To overcome the problem, these markers are deleted temporarily when they are detected as “overlap markers” and restored when the two particles separate.

C. Simulation setup

The present computation is conducted in a rectangular domain with a Cartesian coordinate system, with x , y , and z representing the streamwise, wall-normal, and spanwise directions, respectively. Since the velocity information is transferred between the Eulerian system of the fluid and the Lagrangian system of the particle-surface markers with the regularized delta function of Peskin²⁴ and the particles may freely visit any position of the entire domain, a uniform Cartesian mesh with grid width $\Delta x = \Delta y = \Delta z$ is employed. The periodic boundary condition is applied in the lateral z -direction; a free-slip condition is applied at the top of the domain. The vertical velocity on the top boundary is calculated as follows:

$$\frac{\partial v}{\partial y} = 0. \quad (13)$$

The no-slip condition is applied at the bottom wall. The widely used convective boundary condition³² is applied at the exit of the domain, which is given as follows:

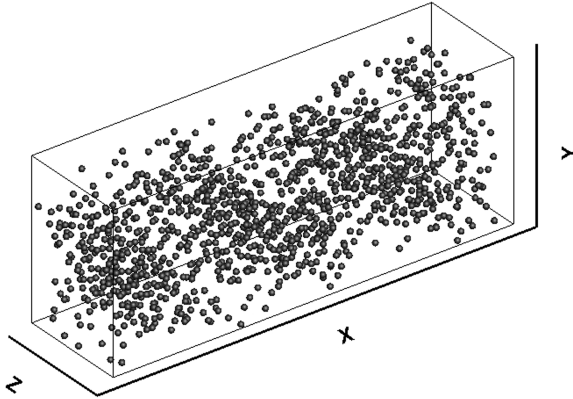


FIG. 1. Geometric configuration of the present simulation and initialized particles.

$$\frac{\partial \mathbf{u}}{\partial t} + U_{conv} \frac{\partial \mathbf{u}}{\partial \mathbf{x}} = 0, \quad (14)$$

where U_{conv} is the mean convective velocity in each direction.

A database extracted from the single-phase data of Wei¹⁶ is used as the inflow boundary condition. The database of Wei¹⁶ is a well-validated ZPGFPTBL, and a time series of the cross-stream plane in the computational domain at the position $Re_0 = 780$ was stored and injected into the present simulation at the inlet. Since the wall-normal grid intervals between the two simulations in the case of Wei¹⁶ are not equal, a 2-D interpolation is adopted to transfer the data from the stretched grid to the uniform grid in the present simulation.

The particles are initially randomly distributed, separated by a distance of at least two diameters from one another, and periodically recirculated in the computational domain in both streamwise and spanwise direction, keeping the solid volume fraction constant throughout the simulation. Particles that are flowing through the outlet are re-injected at same height and depth with same velocity as they flow out of the domain. It is worth noting that, to prevent the influence of recirculated particles to the inlet boundary condition, instead of re-injected exactly at the inlet, particles are injected at a distance of 5 diameters downstream from the inlet. A sketch of the geometry of the domain and the initialized particles is shown in Fig. 1.

As shown in Table I, the uniform mesh width h is approximately 0.92 wall units ($h^+ = 0.92$), and the particle diameter D in the particle-laden case is approximately 11 wall units ($D^+ = 11$), corresponding to approximately $12h$. For the present solid volume fraction (1/1000), 1200 particles are injected into the computational domain of size $534\theta_0 \times 207\theta_0 \times 144\theta_0$ ($x \times y \times z$). As a result of the parameters described above, the total grid number of the present simulation reaches approximately 1.2×10^9 , and the simulation is executed on 600 cores using a message passing interface (MPI) parallelization lasting for over 3 months.

TABLE I. Details of the computational domain.

Case	h^+	N_x	N_y	N_z	ρ_p/ρ_f	N_p
Particle-free	0.92	2138	828	576		
Particle-laden	0.92	2138	828	576	3.3	1200

III. RESULTS AND DISCUSSION

The present simulation is constituted of a single-phase case and a particle-laden case. To investigate the effect of the turbulence modulation caused by finite-sized particles, the results from the two cases are compared, and particle characteristics, such as collision rate, particle velocity, and distribution of number density in the boundary layer, are analyzed.

A. Single-phase data

Figs. 2 and 3 show the time-averaged mean velocity profiles of the single-phase case, normalized with the outer-coordinate and wall units. It can be observed that the averaged mean velocity profiles predicted by the current simulation are in very close agreement with the experimental works of Purtell *et al.*³³ and Murlis *et al.*³⁴ and the simulation work of Spalart.¹⁰ Fig. 4 shows the comparison of the predicted normalized root mean square (r.m.s.) of the fluctuating velocity in three directions at position $Re_0 = 790$ with the results of Erm and Joubert³⁵ and Purtell *et al.*³³ These results demonstrate that the present simulation is accurate in predicting sing-phase flow in the low Reynolds number region.

B. Flow structures

After the full establishment of the single-phase case, particles are randomly added to the fluid field to start calculation of multi-phase case. The simulation of multi-phase case is

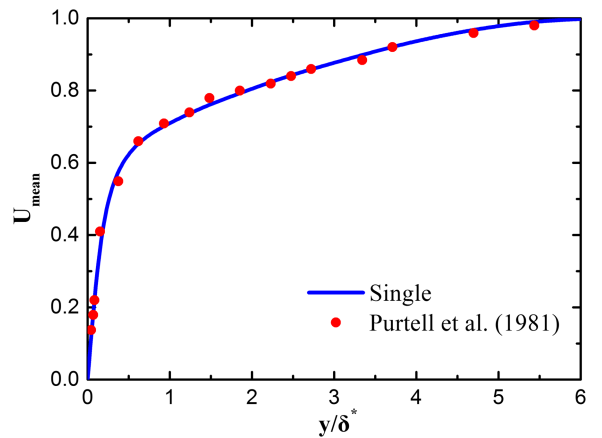


FIG. 2. Mean velocity profile as a function of y/δ^* .

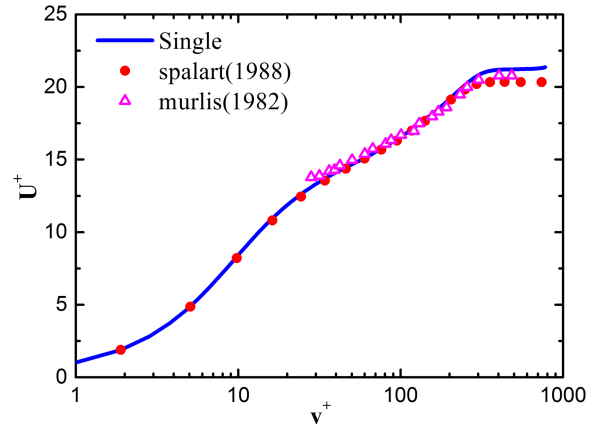


FIG. 3. Mean velocity profile as a function of y^+ .

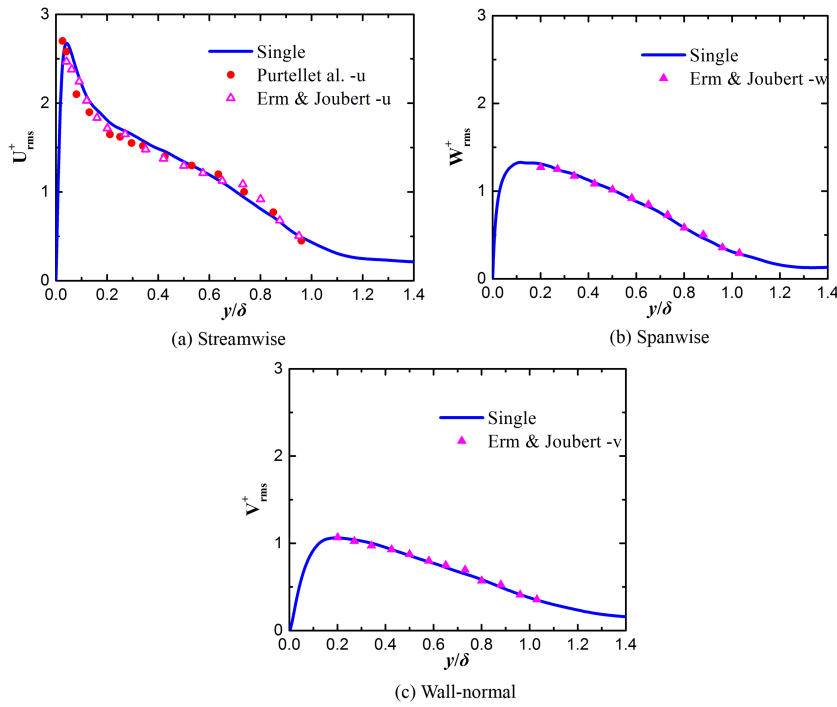
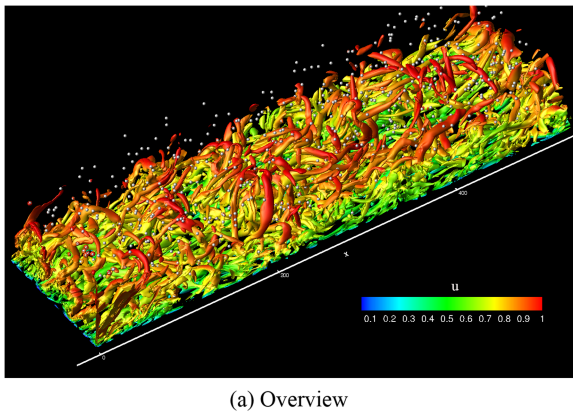


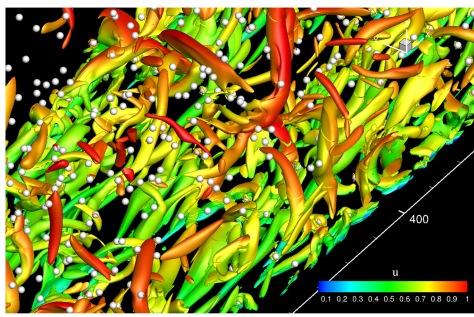
FIG. 4. Turbulence intensities as a function of outer coordinate y/δ .

continued for 30 periods of time ($T = \frac{L_x}{U_\infty}$, where L_x is the length of computational domain in streamwise direction), and the statistics discussed in the following are based on the latter 24 periods.

Fig. 5 depicts the instantaneous fluid-vortex structures colored by streamwise velocity and real-size particles in the computational domain when the boundary layer is fully



(a) Overview



(b) Local zoom

FIG. 5. Vortex structure of the boundary layer in the particle-laden case (white dots are the finite-sized particles and the vortex structure is colored with normalized streamwise velocity).

developed. Typical structures, such as hairpin vortexes or horseshoe vortexes, can be observed along with finite-sized particles. It is also well illustrated that the present particle diameter approximates to the scale of the fluid structure, especially near the wall region.

To better visualize the influence of the presence of the particles on the flow structures, the contours of fluctuating velocity streaks and dissipation rate of turbulent kinetic energy near the wall region ($y^+ = 22$) are plotted in Fig. 6, where the particles are, respectively, colored in black and white. The dissipation rate of turbulent kinetic energy is calculated as follows:

$$\epsilon = 2\sigma_{ij}'\sigma_{ij}', \quad (15)$$

where the strain-rate tensor $\sigma_{ij}' = (u'_{ij} + u'_{ji})/2$.

Since the solid volume fraction is low, particles are dispersed in the fluid and no particle clusters are observed in the figure. As is well known, particle size is a key factor in influencing the interaction between turbulent flow and particle motion.^{7–9} The visualization results based on the particle-resolved show a different result compared with previous simulation study¹⁵ based on point-particle assumption. The results shown in Figs. 6(a) and 6(b) demonstrate that, the tendency of particles to accumulate in the low-speed streak, which has been observed in previous experimental and simulation work,^{6,15,16} does not appear in the present simulation. It is on probably account of the large particle inertia investigated in the present study which was also revealed by Hetsroni and Rozenblit.³⁶ However, as shown in Figs. 6(c) and 6(d), an increased level of turbulent kinetic energy dissipation rate can be observed due to the interaction between the particle surface and fluid.³⁷

C. Fluid statistics

The wall drag exerted by the fluid is usually expressed with non-dimensionalized wall friction coefficients,

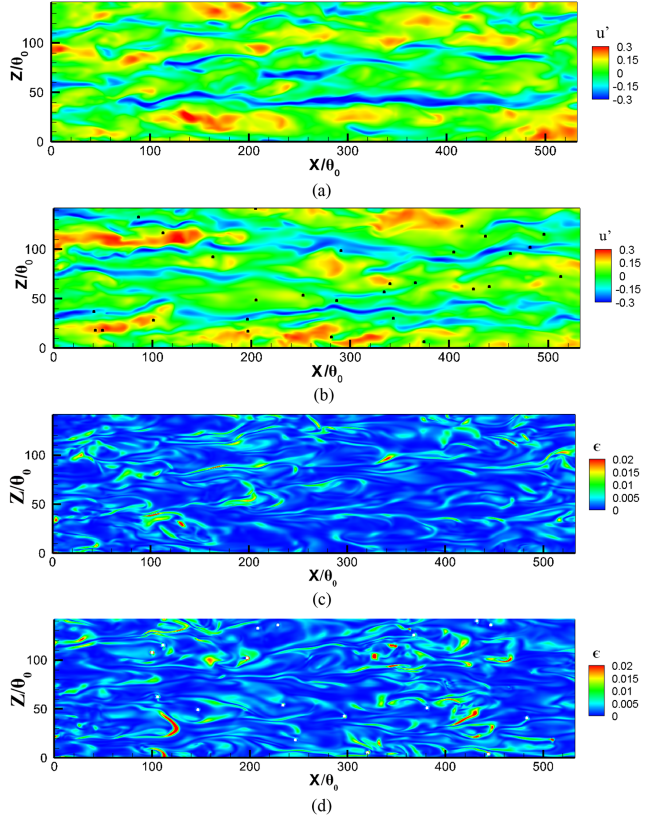


FIG. 6. Contour plots of the (a) single-phase streamwise fluctuating velocity, (b) multi-phase streamwise fluctuating velocity, (c) single-phase dissipation rate of turbulent kinetic energy, (d) multi-phase dissipation rate of turbulent kinetic energy.

$$C_f = \frac{\mu \left(\frac{\partial u}{\partial y} \right)_{y=0}}{\frac{1}{2} \rho U_\infty^2}. \quad (16)$$

Fig. 7 compares the wall friction coefficients along the plate between the two cases. With the addition of the particulate phase, the minimum value of C_f , which corresponds to the onset of the transition,¹¹ is shifted earlier in the streamwise direction. Meanwhile, the peak of C_f curve behind the transition point, which represents the completion of the transition process, is shifted earlier, too. In the middle of the transitional and fully turbulent regions, the friction coefficient with particle-laden phase is increased compared with that of the single phase, which was also reported by Li *et al.*¹⁵

Fig. 8 shows the profiles of the streamwise mean velocity in the single- and multi-phase cases normalized with the

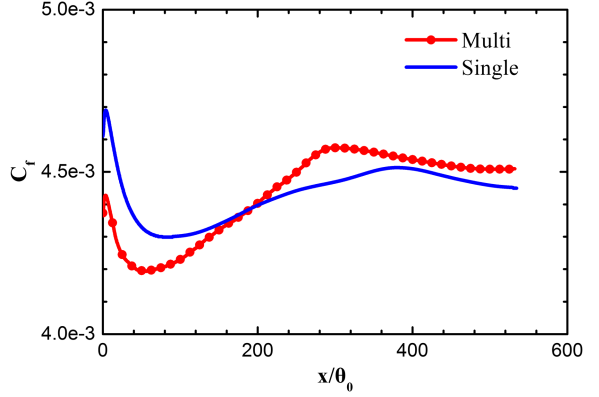


FIG. 7. Comparison of the mean skin-friction coefficient C_f along the domain.

outer and wall scales. No major difference is observed between the two cases, which is consistent with the results of Kulick *et al.*³⁸ and Kidanemariam *et al.*³⁹ It can be concluded that under the present solid volume fraction and solid-fluid density ratio, the modification by the solid phase to the fluid mean velocity can be neglected. The comparison of the r.m.s. of the fluid velocity fluctuations between the single-phase case and the particle-laden case is shown in Fig. 9. It is indicated that the presence of the solid phase has slightly damped the profile, mainly in the wall-normal region of $y^+ < 150$, while little difference is observed in other regions. As illustrated in Figs. 6(c) and 6(d), the damping of the velocity fluctuation is mainly caused by the dissipation adjacent to the particle surfaces.

D. Particle motion in boundary layer

To explain and verify the apparent influential region $y^+ < 150$, instantaneous contour plot of the vorticity across the boundary layer at a random y - z cross section is shown in Fig. 10. The magnitude of vorticity is given as

$$|\omega| = \left| \left(\frac{\partial w}{\partial y} - \frac{\partial v}{\partial z}, \frac{\partial u}{\partial z} - \frac{\partial w}{\partial x}, \frac{\partial v}{\partial x} - \frac{\partial u}{\partial y} \right) \right|. \quad (17)$$

The lengths of the arrows starting from the centers of the particles are proportional to the magnitudes of their cross-stream velocities. It is visually demonstrated that the particles near the wall tend to have higher levels of cross-stream movements due to the momentum transportation from the local streamwise vortexes.

For further investigation, the time-averaged cross-stream velocity profile of particulate phase is plotted in Fig. 11. As

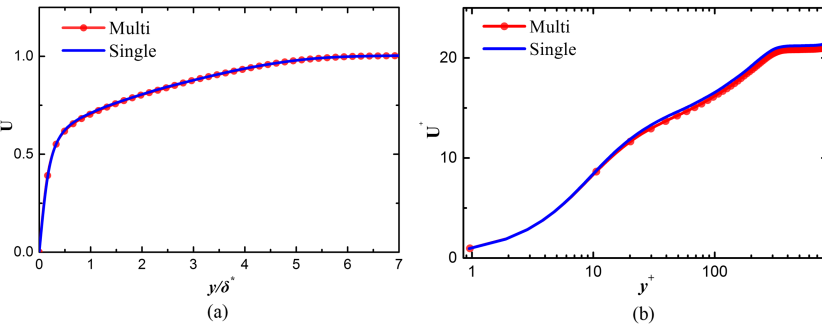


FIG. 8. Comparison of the averaged streamwise velocity in (a) outer units and (b) wall units.

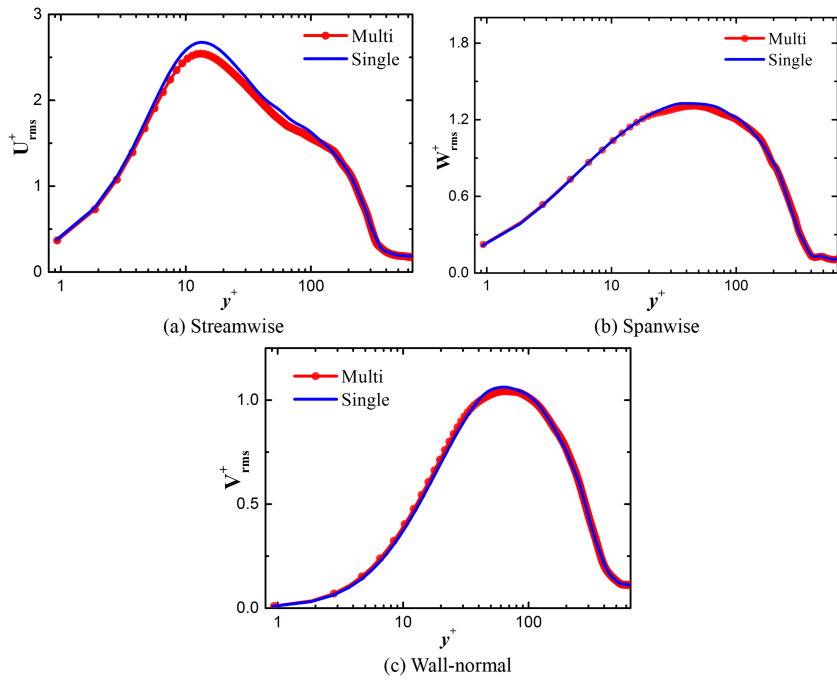


FIG. 9. Comparison of the r.m.s. of the fluctuating velocity.

shown in the figure, higher cross-stream velocities of particles appear in the near-wall region ($30 < y^+ < 150$), where the coherent wall structure plays a dominant role in affecting particle motions.

Another piece of circumstantial evidence is the collision event count as a function of the wall-normal height across the computational domain, which is normalized by the total collision occurrence. As shown in Fig. 12, at the lower height near the bottom wall, a much higher magnitude of collision count is observed compared to the outer region. The

intensive inter-particle collisions are believed to be attributed to the stronger cross-stream particle motion and preferential concentration in this region. As a consequence of the strong movement of the particles in this region, it can be observed in Fig. 10 that, relatively more significant vortexes which correspond to the dissipative shear stresses around the particle surfaces are observed below $y=40$ ($y^+=150$). This proves that the solids have induced an increased amount of turbulent dissipation to the fluid phase in this region.

Fig. 13 compares the time-averaged particle streamwise velocity, which is extracted with discrete bins,⁴⁰ with that of the carrier phase. The lag between particle velocity and the fluid phase exists over the entire range of wall-normal distances. Based on the maximum instantaneous relative velocity, the maximum particle Reynolds number $Re_p = \frac{(\bar{u}_f - \bar{u}_p)_{\max} D_p}{v}$ is approximately 33, so the influence of vortex shedding behind the particle on the turbulence modulation can be neglected. For the wall-normal height $y^+ \approx 20\text{--}40$, a velocity platform is formed, indicating that the particle velocity is very close to

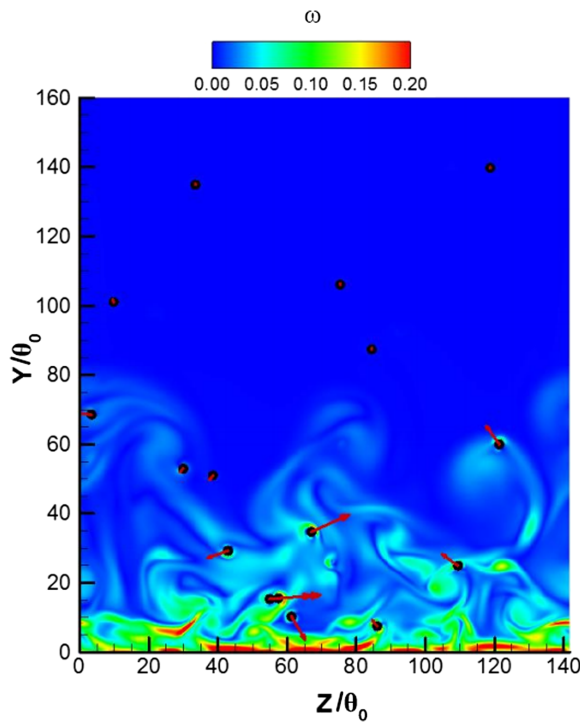


FIG. 10. Contour of the vorticity at a random cross section in the x-direction.

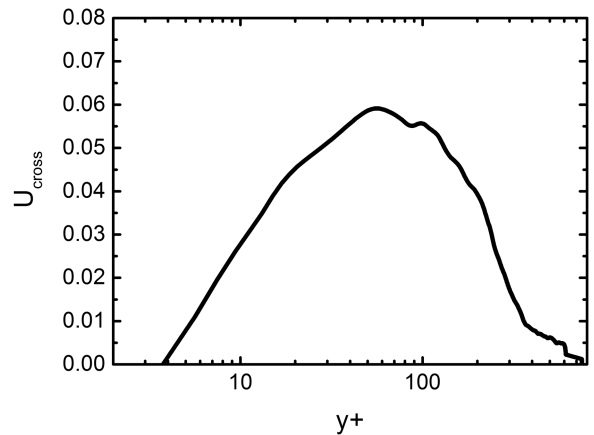


FIG. 11. Time-averaged profile of particle cross-stream particle velocity.

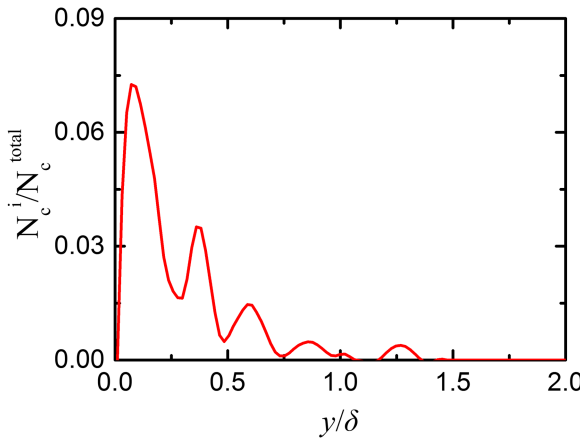


FIG. 12. Collision frequency as a function of the wall-normal distance.

the velocity of the carrier phase, which shows that a higher-speed particle in the outer layer has a greater tendency to move towards the wall.

For further investigation, according to their initial wall-normal coordinates, the particles are extracted into four groups of $y^+ = (20–60]$, $(60–120]$, $(120–211]$, and $(211–315]$. Based on the instantaneous coordinates of the particles throughout the simulation, the PDFs (probability density function) of their wall-normal positions are shown in Fig. 14. The PDF describes the spatial distribution of particles, which is calculated as follows:

$$\text{PDF}(y_1 < y^+ < y_1 + \Delta y) = \frac{N_{p,y_1 \sim y_1 + \Delta y}}{N_{p,\text{total}} \times \Delta y}, \quad (18)$$

where $N_{p,y_1 \sim y_1 + \Delta y}$ is number of particles located at range of $y_1 < y^+ < y_1 + \Delta y$ and $N_{p,\text{total}}$ is the particle number in the corresponding group.

By comparing the four profiles, the same tendencies for particles to concentrate between $y^+ \approx 20–30$ and avoid the region $y^+ \approx 40–60$, as a result of the turbophoresis effect,^{41,42} are observed. The four profiles also show that the particles that originated in the ranges $(60–120]$ and $(120–211]$ are the most influenced by this effect during the simulation. Therefore, it can be concluded that the fore-mentioned velocity platform at $y^+ \approx 20–40$ in Fig. 13 is formed by the downward penetration of the outer-layer particles located at $y^+ \approx (60–315]$. It is also very interesting that some of the particles that were initially very close to the wall can be transported to the outside of the

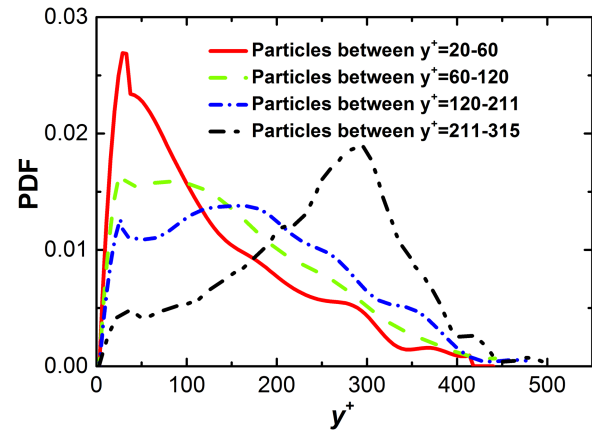


FIG. 14. PDF of the distribution density as a function of wall-normal distance.

boundary layer, up to region $y^+ \approx 400$, and vice versa for the particles that were initially in the outer region.

IV. CONCLUSION

Direct numerical simulation of a turbulent boundary layer laden with fully resolved particles is conducted for the first time. The solids are represented using the immersed-boundary method, and a soft-sphere collision model is applied to prevent the rigid particles from penetrating one another.

Due to the dilute concentration, the mean velocity of the boundary layer is almost undisturbed by the particles, while the whole transition process is shifted earlier. Compared to the outer-layer regions, much higher levels of spanwise movement and collision occurrence for the particles are observed in the near-wall region due to the transportation of the streamwise vortexes, hence increasing the turbulent dissipation on the particle surfaces and reducing the r.m.s. of the turbulent fluctuating velocity in all three directions.

Since the particle inertias studied are much larger than the particles simulated using the point-particle assumption, an apparent velocity lag with respect to the carrier phase exists throughout the boundary layer. For this reason, the maximum particle Reynolds number is very small; hence, no vortex shedding is present. A trajectory analysis of the particles shows the influence of turbophoresis on particle wall-normal concentration, and the particles that originated between $y^+ = 60$ and $2/3$ of the boundary-layer thickness are the most influenced.

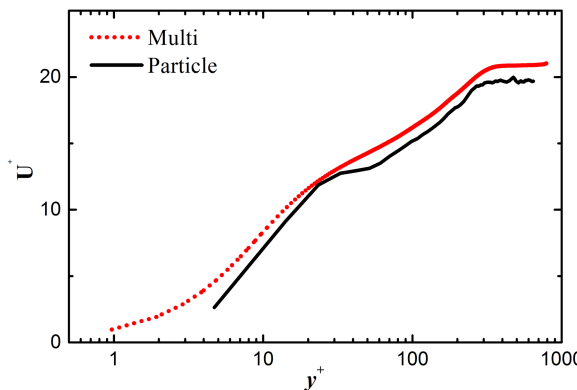


FIG. 13. Comparison of the particle mean velocity with that of the fluid phase.

ACKNOWLEDGMENTS

Financial supports from the National Natural Science Foundations of China (Grant No. 51390491) is sincerely acknowledged.

¹F. Lee and F. C. Lockwood, "Modelling ash deposition in pulverized coal-fired applications," *Prog. Energy Combust. Sci.* **25**, 117–132 (1999).

²M. Y. Louge, E. Mastorakos, and J. T. Jenkins, "The role of particle collisions in pneumatic transport," *J. Fluid Mech.* **231**, 345–359 (1991).

³B. Westrich and U. Forstner, *Sediment Dynamics and Pollutant Mobility in Rivers: An Interdisciplinary Approach* (Springer Science & Business Media, 2007).

⁴M. Rashidi, G. Hetsroni, and S. Banerjee, "Particle-turbulence interaction in a boundary layer," *Int. J. Multiphase Flow* **16**, 935–949 (1990).

- ⁵C. B. Rogers and J. K. Eaton, "The effect of small particles on fluid turbulence in a flat-plate, turbulent boundary layer in air," *Phys. Fluids A* **3**, 928–937 (1991).
- ⁶D. Kaftori, G. Hetsroni, and S. Banerjee, "Particle behavior in the turbulent boundary layer. I. Motion, deposition, and entrainment," *Phys. Fluids* **7**, 1095–1106 (1995).
- ⁷D. Kaftori, G. Hetsroni, and S. Banerjee, "Particle behavior in the turbulent boundary layer. II. Velocity and distribution profiles," *Phys. Fluids* **7**, 1107–1121 (1995).
- ⁸Y. Tsuji and Y. Morikawa, "LDV measurements of an air-solid two-phase flow in a horizontal pipe," *J. Fluid Mech.* **120**, 385–409 (1982).
- ⁹Y. Tsuji, Y. Morikawa, and H. Shiomi, "LDV measurements of an air-solid two-phase flow in a vertical pipe," *J. Fluid Mech.* **139**, 417–434 (1984).
- ¹⁰P. R. Spalart, "Direct simulation of a turbulent boundary layer up to $R_0 = 1410$," *J. Fluid Mech.* **187**, 61–98 (1988).
- ¹¹X. Wu and P. Moin, "Direct numerical simulation of turbulence in a nominally zero-pressure-gradient flat-plate boundary layer," *J. Fluid Mech.* **630**, 5–41 (2009).
- ¹²G. Borrell, J. A. Sillero, and J. Jiménez, "A code for direct numerical simulation of turbulent boundary layers at high Reynolds numbers in BG/P supercomputers," *Comput. Fluids* **80**, 37–43 (2013).
- ¹³G. Sardina, P. Schlatter, F. Picano, C. M. Casciola, L. Brandt, and D. S. Henningson, "Self-similar transport of inertial particles in a turbulent boundary layer," *J. Fluid Mech.* **706**, 584–596 (2012).
- ¹⁴Y. Yamamoto, M. Potthoff, T. Tanaka, T. Kajishima, and Y. Tsuji, "Large-eddy simulation of turbulent gas-particle flow in a vertical channel: Effect of considering inter-particle collisions," *J. Fluid Mech.* **442**, 303–334 (2001).
- ¹⁵D. Li, A. Wei, K. Luo, and J. Fan, "Direct numerical simulation of a particle-laden flow in a flat plate boundary layer," *Int. J. Multiphase Flow* **79**, 124–143 (2016).
- ¹⁶A. Wei, "Direct numerical simulation of turbulent boundary layer," Ph.D. dissertation (Zhejiang University, 2015).
- ¹⁷S. K. Lele, "Compact finite difference schemes with spectral-like resolution," *J. Comput. Phys.* **103**, 16–42 (1992).
- ¹⁸Y. Zhuang and X. Sun, "A high-order fast direct solver for singular Poisson equations," *J. Comput. Phys.* **171**, 79–94 (2001).
- ¹⁹A. Jameson and W. Schmidt, "Some recent developments in numerical methods for transonic flows," *Comput. Methods Appl. Mech. Eng.* **51**, 467–493 (1985).
- ²⁰E. A. Fadlun, R. Verzicco, P. Orlandi, and J. Mohd-Yusof, "Combined immersed-boundary finite-difference methods for three-dimensional complex flow simulations," *J. Comput. Phys.* **161**, 35–60 (2000).
- ²¹J. Kim, D. Kim, and H. Choi, "An immersed-boundary finite-volume method for simulations of flow in complex geometries," *J. Comput. Phys.* **171**, 132–150 (2001).
- ²²Y. H. Tseng and J. H. Ferziger, "A ghost-cell immersed boundary method for flow in complex geometry," *J. Comput. Phys.* **192**, 593–623 (2003).
- ²³E. Balaras, "Modeling complex boundaries using an external force field on fixed Cartesian grids in large-eddy simulations," *Comput. Fluids* **33**, 375–404 (2004).
- ²⁴C. S. Peskin, "The immersed boundary method," *Acta Numer.* **11**, 479–517 (2001).
- ²⁵K. Luo, Z. Wang, and J. Fan, "Response of force behaviors of a spherical particle to an oscillating flow," *Phys. Lett. A* **374**, 3046–3052 (2010).
- ²⁶Z. Wang, J. Fan, and K. Cen, "Immersed boundary method for the simulation of 2D viscous flow based on vorticity–velocity formulations," *J. Comput. Phys.* **228**, 1504–1520 (2009).
- ²⁷Z. Wang, J. Fan, and K. Luo, "Combined multi-direct forcing and immersed boundary method for simulating flows with moving particles," *Int. J. Multiphase Flow* **34**, 283–302 (2008).
- ²⁸B. E. Griffith and C. S. Peskin, "On the order of accuracy of the immersed boundary method: Higher order convergence rates for sufficiently smooth problems," *J. Comput. Phys.* **208**, 75–105 (2005).
- ²⁹Y. Tsuji, T. Kawaguchi, and T. Tanaka, "Discrete particle simulation of two-dimensional fluidized bed," *Powder Technol.* **77**, 79–87 (1993).
- ³⁰B. Hoomans, J. Kuipers, W. J. Briels, and W. Van Swaaij, "Discrete particle simulation of bubble and slug formation in a two-dimensional gas-fluidised bed: A hard-sphere approach," *Chem. Eng. Sci.* **51**, 99–118 (1996).
- ³¹L. E. Silbert, D. Ertas, G. S. Grest, T. C. Halsey, D. Levine, and S. J. Plimpton, "Granular flow down an inclined plane: Bagnold scaling and rheology," *Phys. Rev. E* **64**, 051302 (2001).
- ³²I. Orlanski, "A simple boundary condition for unbounded hyperbolic flows," *J. Comput. Phys.* **21**, 251–269 (1976).
- ³³L. P. Purtell, P. S. Klebanoff, and F. T. Buckley, "Turbulent boundary layer at low Reynolds number," *Phys. Fluids* **24**, 802–811 (1981).
- ³⁴J. Murlis, H. M. Tsai, and P. Bradshaw, "The structure of turbulent boundary layers at low Reynolds numbers," *J. Fluid Mech.* **122**, 13–56 (1982).
- ³⁵L. P. Erm and P. N. Joubert, "Low-Reynolds-number turbulent boundary layers," *J. Fluid Mech.* **230**, 1–44 (1991).
- ³⁶G. Hetsroni and R. Rozenblit, "Heat transfer to a liquid—Solid mixture in a flume," *Int. J. Multiphase Flow* **20**, 671–689 (1994).
- ³⁷S. Balachandar and J. K. Eaton, "Turbulent dispersed multiphase flow," *Annu. Rev. Fluid Mech.* **42**, 111–133 (2010).
- ³⁸J. D. Kulick, J. R. Fessler, and J. K. Eaton, "Particle response and turbulence modification in fully developed channel flow," *J. Fluid Mech.* **277**, 109–134 (1994).
- ³⁹A. G. Kidanemariam, C. Chan-Braun, T. Doychev, and M. Uhlmann, "Direct numerical simulation of horizontal open channel flow with finite-size, heavy particles at low solid volume fraction," *New J. Phys.* **15**, 025–031 (2013).
- ⁴⁰M. Uhlmann, "Interface-resolved direct numerical simulation of vertical particulate channel flow in the turbulent regime," *Phys. Fluids* **20**, 053305 (2008).
- ⁴¹M. Caporaloni, F. Tampieri, F. Trombetti, and O. Vittori, "Transfer of particles in nonisotropic air turbulence," *J. Atmos. Sci.* **32**, 565–568 (1975).
- ⁴²M. W. Reeks, "The transport of discrete particles in inhomogeneous turbulence," *J. Aerosol Sci.* **14**, 729–739 (1983).